nanomaterials

MDPI

Article

Broadband Optical Constants and Nonlinear Properties of SnS_2 and $SnSe_2$

Georgy A. Ermolaev [1], Dmitry I. Yakubovsky [1], Marwa A. El-Sayed [1,2], Mikhail K. Tatmyshevskiy [1], Arslan B. Mazitov [1,3], Anna A. Popkova [4], Ilya M. Antropov [4], Vladimir O. Bessonov [4], Aleksandr S. Slavich [1], Gleb I. Tselikov [1], Ivan A. Kruglov [1,3], Sergey M. Novikov [1], Andrey A. Vyshnevyy [1], Andrey A. Fedyanin [4], Aleksey V. Arsenin [1] and Valentyn S. Volkov [1,*]

[1] Center for Photonics and 2D Materials, Moscow Institute of Physics and Technology, 9 Institutsky Lane, 141700 Dolgoprudny, Russia; georgiy.ermolayev@phystech.edu (G.A.E.); dmitrii.yakubovskii@phystech.edu (D.I.Y.); mira@phystech.edu (M.A.E.-S.); mikhail.tatmyshevskiy@phystech.edu (M.K.T.); arslan.mazitov@phystech.edu (A.B.M.); slavich.as@phystech.edu (A.S.S.); celikov@physics.msu.ru (G.I.T.); kruglov.ia@mipt.ru (I.A.K.); novikov.s@mipt.ru (S.M.N.); andrey.vyshnevyy@phystech.edu (A.A.V.); arsenin.av@mipt.ru (A.V.A.)

[2] Department of Physics, Faculty of Science, Menoufia University, Shebin El-Koom 32511, Egypt

[3] Dukhov Research Institute of Automatics (VNIIA), 22 Suschevskaya St., 127055 Moscow, Russia

[4] Faculty of Physics, Lomonosov Moscow State University, 119991 Moscow, Russia; popkova@nanolab.phys.msu.ru (A.A.P.); antropov@nanolab.phys.msu.ru (I.M.A.); bessonov@nanolab.phys.msu.ru (V.O.B.); fedyanin@nanolab.phys.msu.ru (A.A.F.)

* Correspondence: volkov.vs@mipt.ru or vsv.mipt@gmail.com; Tel.: +7-926-735-93-98

Abstract: SnS_2 and $SnSe_2$ have recently been shown to have a wide range of applications in photonic and optoelectronic devices. However, because of incomplete knowledge about their optical characteristics, the use of SnS_2 and $SnSe_2$ in optical engineering remains challenging. Here, we addressed this problem by establishing SnS_2 and $SnSe_2$ linear and nonlinear optical properties in the broad (300–3300 nm) spectral range. Coupled with the first-principle calculations, our experimental study unveiled the full dielectric tensor of SnS_2 and $SnSe_2$. Furthermore, we established that SnS_2 is a promising material for visible high refractive index nanophotonics. Meanwhile, $SnSe_2$ demonstrates a stronger nonlinear response compared with SnS_2. Our results create a solid ground for current and next-generation SnS_2- and $SnSe_2$-based devices.

Keywords: two-dimensional materials; optical constants; dielectric properties; refractive index; nanophotonics; spectroscopic ellipsometry; second harmonic generation

Citation: Ermolaev, G.A.; Yakubovsky, D.I.; El-Sayed, M.A.; Tatmyshevskiy, M.K.; Mazitov, A.B.; Popkova, A.A.; Antropov, I.M.; Bessonov, V.O.; Slavich, A.S.; Tselikov, G.I.; et al. Broadband Optical Constants and Nonlinear Properties of SnS_2 and $SnSe_2$. *Nanomaterials* **2022**, *12*, 141. https://doi.org/10.3390/nano12010141

Academic Editor: Bingsuo Zou

Received: 5 December 2021
Accepted: 28 December 2021
Published: 31 December 2021

1. Introduction

Van der Waals materials have emerged as a promising building block for next-generation optical and electronic devices [1–8]. Their planar structure [9,10] and the outstanding compatibility with existing manufacturing techniques [11–15] make such materials ideal for integration into modern industrial and scientific devices. Among layered materials, graphene [16], MoS_2 [17], and hBN [18] have received the most attention, as they were the first [19–21] to catch researchers' interest during the "two-dimensional" revolution [22] in material science. However, the number of known layered materials has increased exponentially over the last decade, with more than 1000 layered compounds being isolated and identified [23]. As a result, their properties are largely unexplored, which considerably impedes their application. In particular, the optical properties of tin-based dichalcogenides SnS_2 and $SnSe_2$ [24,25] are mostly unknown, with rare reports [26–30] on their absorption properties. Nonetheless, SnS_2 and $SnSe_2$ have already demonstrated their huge potential in optoelectronic applications, such as field-effect transistors [31–33], solar cells [34,35], saturable absorbers [36–38], photonic crystals [39,40], and photodetectors [41,42]. Hence, broadband linear and nonlinear optical

properties are highly desired for the acceleration of the development of SnS_2 and $SnSe_2$-based devices.

Here, the objective of the present work is the comprehensive optical characterization of SnS_2 and $SnSe_2$. Using spectroscopic ellipsometry and first-principle calculations, we determine the full broadband dielectric tensor of SnS_2 and $SnSe_2$ from ultraviolet to mid-infrared wavelengths (300–3300 nm). The results demonstrate a high dielectric response ($n > 3$) with zero losses in a wide spectral range: 560–3300 nm for SnS_2 and 1300–3300 nm for $SnSe_2$. Moreover, we measured the second-order nonlinear optical susceptibility of SnS_2 and $SnSe_2$ at wavelengths ranging from 750 to 1050 nm. Finally, our results revealed that SnS_2 is a high refractive index material, which fills the important gap in the visible spectrum between bandgap energies of GaP and TiO_2, which makes SnS_2 a promising material for all-dielectric nanophotonics.

2. Results and Discussion

2.1. Surface and Structural Morphology Study

Thin films of SnS_2 and $SnSe_2$ were synthesized by the chemical vapor deposition (CVD) method and transferred on a quartz substrate. Figure 1a schematically illustrates the crystal structure of 1T-SnS_2 or $SnSe_2$ viewed along *c*- axis and the *a*-axis. This crystal configuration is the most common atoms' arrangement for SnS_2 and $SnSe_2$, where layers stack directly above one another [43,44]. Optical microscopy photographs in Figure 1b,f show the uniform substrate's coverage of synthesized SnS_2 and $SnSe_2$ films. Likewise, scanning electron microscopy (SEM) images in Figure 1c,g confirm the films' full-area coverage and homogeneity at the microscale. In addition, we checked the films' surface by atomic force microscopy (AFM), demonstrating an atomically smooth surface with root mean square (RMS) roughness of less than 1.6 nm and 0.5 nm for SnS_2 and $SnSe_2$, respectively. Ultimately, we accurately measured the films' thickness via AFM topographical scans (Figure 1e,i). They yielded 20.0 ± 1.8 nm and 6.5 ± 0.7 nm thicknesses for SnS_2 and $SnSe_2$ films, correspondingly.

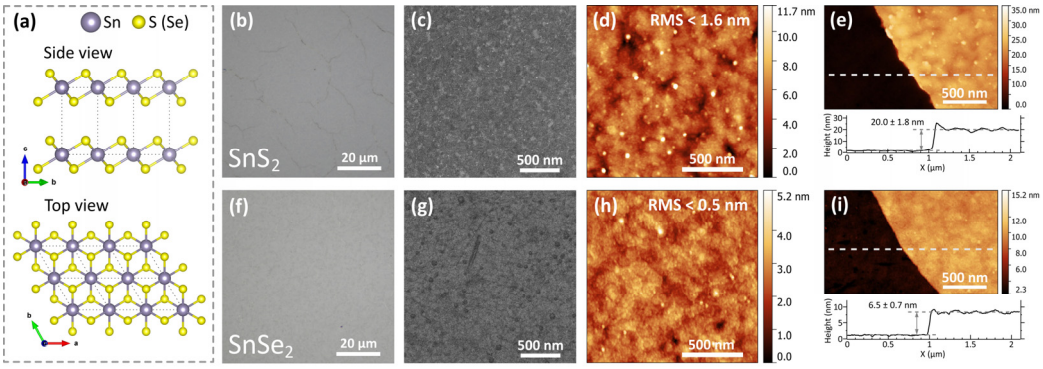

Figure 1. Morphology of SnS_2 and $SnSe_2$. (**a**) Crystal lattice structure of 1T-SnS_2 (or 1T-$SnSe_2$) [44], optical microscopy images of (**b**) SnS_2 and (**f**) $SnSe_2$. SEM images of (**c**) SnS_2 and (**g**) $SnSe_2$. AFM scan images of (**d**) SnS_2 and (**h**) $SnSe_2$. AFM thickness measurements of (**e**) SnS_2 and (**i**) $SnSe_2$ films with characteristic step height profiles.

2.2. Analysis of the Crystal Structure and Raman Characterization

In nature, SnS_2 and $SnSe_2$ exist in several phase modifications [45,46], including 1T, 2H, 4H, and 18R polytypes. To identify the phase of our samples, we performed X-ray diffraction (XRD), whose spectra are displayed in Figure 2a,b. According to the Joint Committee on Powder Diffraction Standards (card No. 23-0677 and 89-2939) and previous publications [27,47,48], the obtained XRD patterns reveal the hexagonal lattice configuration, which could be 1T or 2H, for SnS_2 and $SnSe_2$ with lattice parameters $a = b = 3.6486$ Å and $c = 5.8992$ Å for SnS_2 and $a = b = 3.811$ Å and $c = 6.137$ Å for $SnSe_2$.

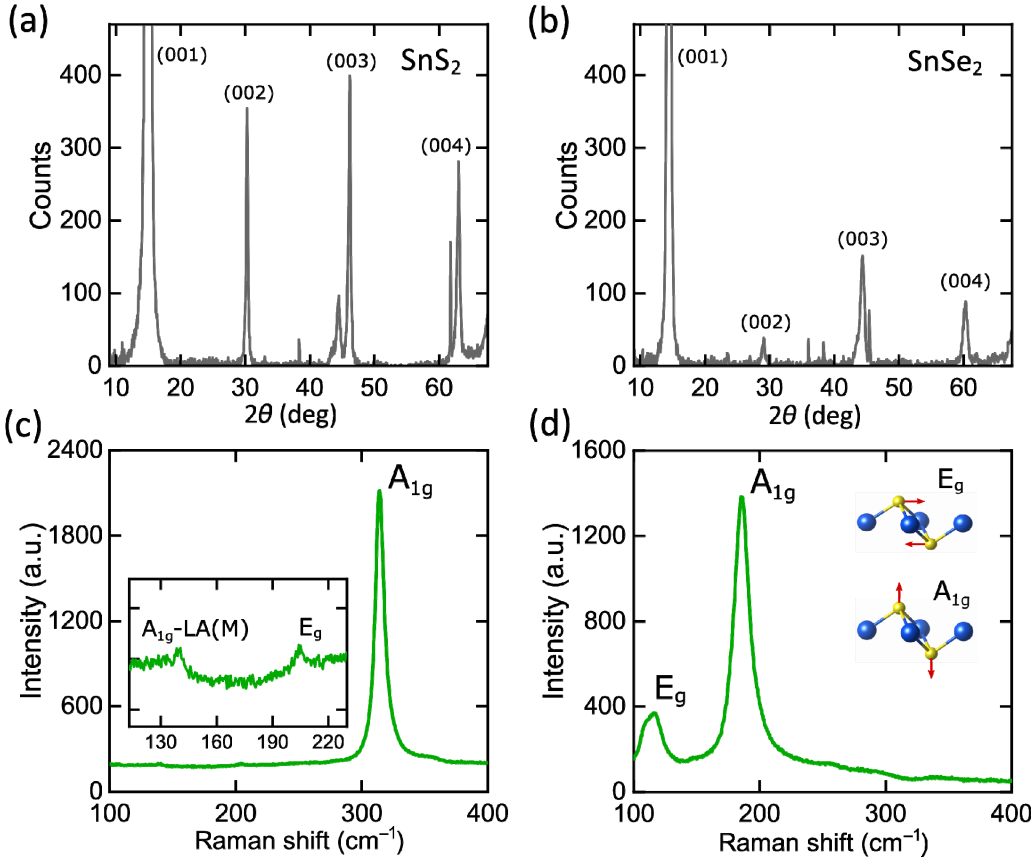

Figure 2. Structural characterization of SnS_2 and $SnSe_2$. XRD patterns of (**a**) SnS_2 and (**b**) $SnSe_2$. Raman spectra for (**c**) SnS_2 and (**d**) $SnSe_2$ thin films.

Aside from XRD characterization, we utilized Raman spectroscopy at 532 nm excitation wavelength (Figure 2c,d) to distinguish between two hexagonal configurations, 1T and 2H. Raman spectrum of SnS_2 reveals out-of-plane vibration mode A_{1g} at ~314 cm^{-1} and in-plane vibration of E_g at ~205 cm^{-1}, corresponding to 1T polytype [44,49,50]. Similar to SnS_2, $SnSe_2$ Raman spectrum has two characteristic phonon modes: A_{1g} mode at ~185 cm^{-1} and E_g mode at ~116.5 cm^{-1}, associated with 1T-phase [36,51]. Moreover, Raman spectra at numerous locations of our samples demonstrate the same A_{1g} and E_g peak positions, additionally validating the homogeneity of the studied SnS_2 and $SnSe_2$ thin films.

2.3. Optical Properties of SnS_2 and $SnSe_2$ Films

We investigated broadband optical constants of SnS_2 and $SnSe_2$ films through spectroscopic ellipsometry. We employed a two-layer optical model for ellipsometry data analysis: quartz substrate with SnS_2 or $SnSe_2$ film with the thickness determined from AFM (Figure 3e,i). Similar to other TMDCs [52,53], we describe SnS_2 and $SnSe_2$ dielectric function by the Tauc–Lorentz oscillator model (see Methods) [54,55]. Figure 3a,b shows the resulting optical constants n and k for SnS_2 and $SnSe_2$ films. Interestingly, we did not observe excitons for SnS_2 and $SnSe_2$, which can be explained by their indirect bandgap, in contrast, to the direct bandgap in MoS_2 and WS_2 [56,57]. Apart from the dielectric function, Tauc–Lorentz oscillator parameters allow us to obtain the positions of critical points of joint density of states: 3.91 eV (317 nm) for SnS_2; 2.87 eV (432 nm) and 3.98 eV (311 nm) for $SnSe_2$. Furthermore, SnS_2 and $SnSe_2$ both have zero absorption ($k \sim 0$) at a broad wavelength range, starting from 560 and 1300 nm (Figure 3a,b), respectively. For reference, we also plotted in Figure 3a,b refractive indices and bandgap transitions of SnS_2 and $SnSe_2$, determined by Domingo and coworkers [26]. As expected, the fundamental absorption edge coincides with the forbidden indirect transitions (Figure 3a,b), supporting our results in Figure 3a,b.

For additional verification, we also measured the transmittance spectra of our samples (Figure 3c,d) and compared them with the transfer matrix calculations [58], based on optical constants from Figure 3a,b. Evidently, calculated and measured transmittance agree well, thereby validating our n and k in Figure 3a,b.

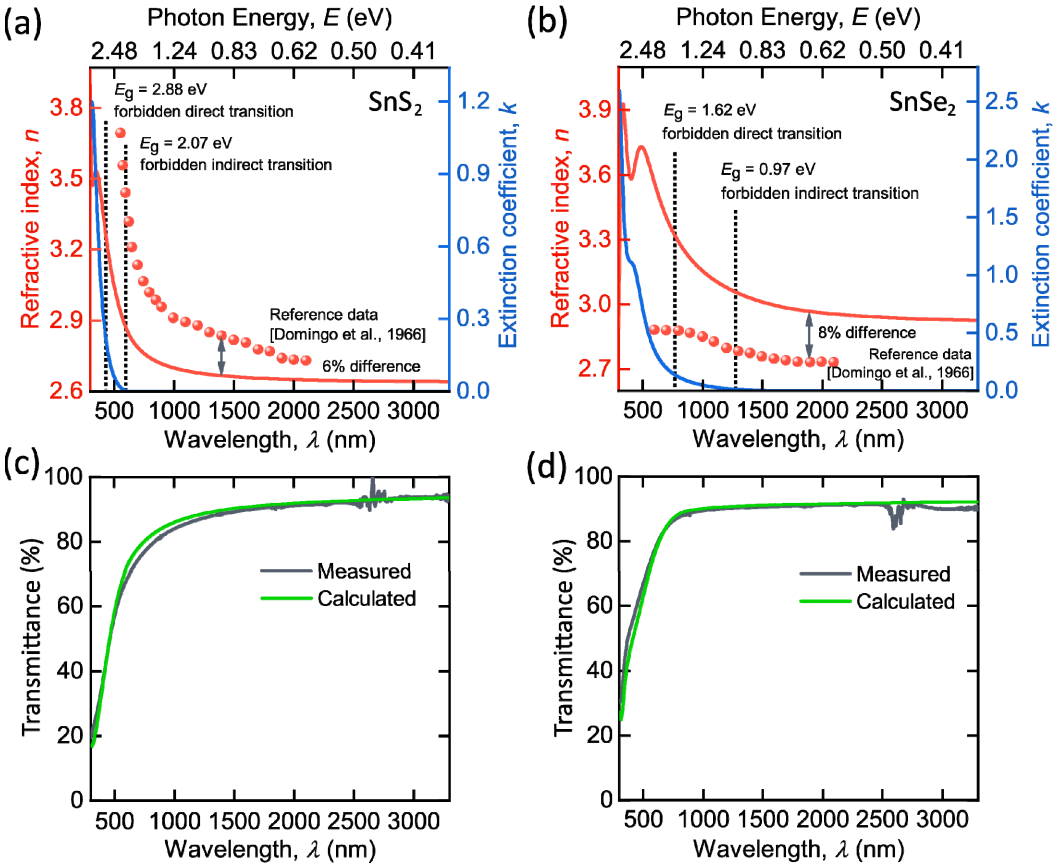

Figure 3. Linear optical properties of SnS_2 and $SnSe_2$**.** Dielectric function of (**a**) SnS_2 and (**b**) $SnSe_2$. For comparison, we included refractive indices (red circles) and electronic transitions (dashed lines) determined by Domingo et al. [26]. Measured and calculated transmittance for (**c**) SnS_2 and (**d**) $SnSe_2$ on quartz. Tabulated optical constants for SnS_2 and $SnSe_2$ are collected in Table A1.

To retrieve the full dielectric tensor, we leveraged first-principle calculations (Methods). Figure 4 shows the resulting refractive index and extinction coefficient along the *ab*-plane (n_{ab} and k_{ab}) and *c*-axis (n_c and k_c). The first-principle calculations reproduce the shape of the experimental dielectric function and render the major optical features: a wide zero-absorption spectral range and high dielectric response. However, first-principle calculations overestimate values of dielectric function since the computations were performed assuming the ideal crystalline structure, whereas the studied CVD-grown films have a polycrystalline structure. Nevertheless, first-principle calculations provide access to the full dielectric permittivity tensor, allowing us to estimate the anisotropic optical properties, which are the most noticeable for SnS_2 with birefringence $\Delta n = n_{ab} - n_c \approx 0.3$ and almost negligible for $SnSe_2$. In contrast, ellipsometry is nearly insensitive to optical constants along the *c*-axis, as explained by Ermolaev and colleagues [56,59]. Thus, our computations reveal for the first time the optical anisotropy in SnS_2 and $SnSe_2$, which could be relevant in next-generation anisotropic nanophotonics [60].

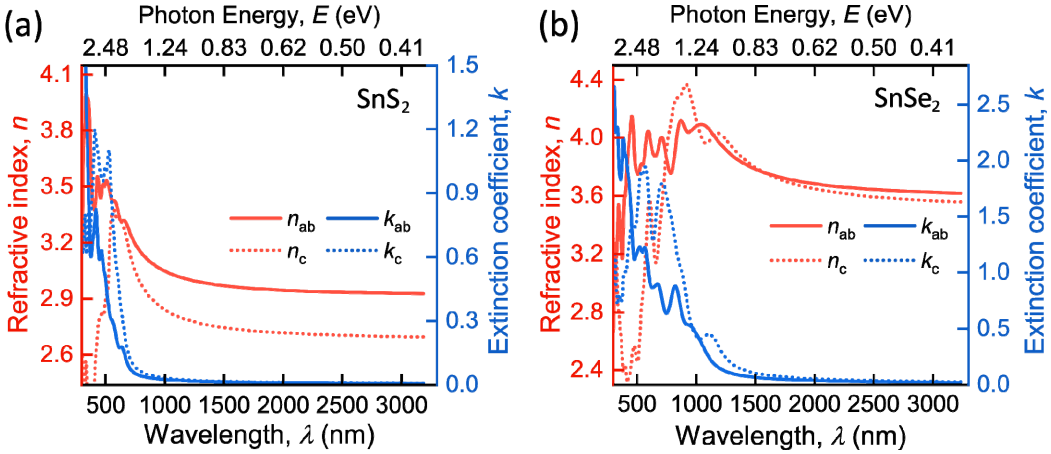

Figure 4. First-principle calculations of SnS_2 and $SnSe_2$**.** Optical constants for (**a**) SnS_2 and (**b**) $SnSe_2$, including in-plane n_{ab}, k_{ab} and out-of-plane n_c, k_c parts of dielectric tensor.

In the light of the rapid development of nonlinear optical devices based on SnS_2 and $SnSe_2$ [36,37,61], we also measured their nonlinear optical response (Figure 5). Specifically, we measured the second harmonic generation (SHG) in transmission geometry using 150 fs laser pulses focused into a 50 µm spot in diameter (see Methods). Figure 5a shows the SHG power dependence with the expected slope of 2 (2.01 ± 0.02 for SnS_2 and 2.02 ± 0.04 for $SnSe_2$), confirming the second-order nonlinear process and the absence of saturation effects. SHG spectra of SnS_2 and $SnSe_2$ are shown in Figure 5b. For $SnSe_2$, SHG resonance is at 415 nm (2.98 eV), associated with the 2 photon direct transition at the critical point (2.87 eV) found above from ellipsometry measurements. The presence of SH signal at large pump wavelengths indicates the contribution of direct transitions with lower energies, meaning that the direct transition of $SnSe_2$ is less than 2.36 eV. In contrast, for SnS_2, the SH signal is negligible at large wavelengths. Therefore, the SHG resonance observed at the SH wavelength of 420 nm (2.95 eV) can be associated with the lowest energy direct transition of SnS_2 in agreement with Domingo and colleagues' work [26].

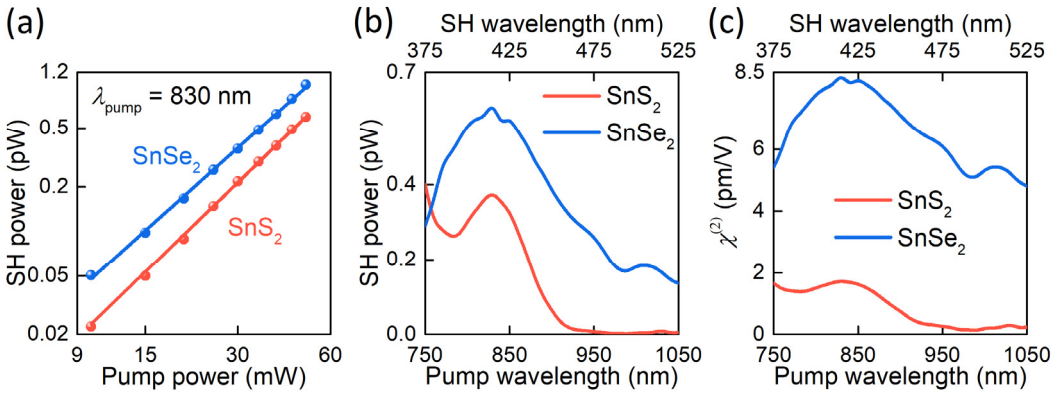

Figure 5. Nonlinear optical properties of SnS_2 and $SnSe_2$. (**a**) Power-dependent nonlinear optical response of SnS_2 and $SnSe_2$ thin films, plotted in double logarithmic scale, and its linear approximation with slope p = 2.01 ± 0.02 for SnS_2 and p = 2.02 ± 0.04 for $SnSe_2$. Pump wavelength is 830 nm. (**b**) SHG spectroscopy of SnS_2 (red line) and $SnSe_2$ (blue line) thin films at 40 mW pump power. (**c**) Wavelength-dependent, second-order, nonlinear optical susceptibility of SnS_2 (red line) and $SnSe_2$ (blue line).

To calculate the nonlinear optical susceptibility, we implemented the method, described in Boyd's book [62]. The technique relies on the following equation for the average power of SHG transmitted through sample:

$$P(2\omega) = \frac{16\sqrt{2}\left|\chi^{(2)}\right|_2 \pi S P^2(\omega) L^2}{\epsilon_0 r^2 f \tau c n_\omega^2 n_{2\omega} \lambda^2} \sin c^2\left(\frac{\Delta k L}{2}\right) \quad (1)$$

where $\chi^{(2)}$ is a nonlinear optical susceptibility, $S = 0.94$ is the shape factor for Gaussian pulses, ϵ_0 is the permittivity of vacuum, c is the speed of light, $f = 80$ MHz is the pulse repetition rate, $\tau = 150$ fs is the pulse duration, $r = 25$ µm is the focal spot radius, L is a sample thickness, λ is a pump wavelength, Δk is the wavevectors mismatch of the pump and SH waves, n_ω and $n_{2\omega}$ are refractive indices of material at pump and harmonic wavelengths, and $P(\omega)$ and $P(2\omega)$ are average power of the pump and the second harmonic radiation, respectively. In our case, the coherence length $L_{coh} = \lambda/(4n_{2\omega} - 4n_\omega)$ of the observed processes is several hundred nanometers (from 300 nm to 900 nm for SnS_2 and from 450 to 600 nm for $SnSe_2$), which significantly exceeds the thickness of the films (Figure 1e,f). Thus, we can assume that the SHG is phase-matched and, hence, $\sin c^2(\Delta k L/2) = 1$. It allows us to evaluate SnS_2 and $SnSe_2$ nonlinear optical susceptibility, displayed in Figure 5c.

Finally, we want to underline that SnS_2 is a promising material for all-dielectric nanophotonics [63,64], demanding a high refractive index and low absorption. As shown in Figure 6, SnS_2 meets both requirements since it possesses a refractive index $n \approx 2.8$ and zero extinction in the visible and infrared ranges. More importantly, SnS_2 could even compete with classical high refractive index materials such as Si, GaP, and TiO_2 [65–68]. In particular, SnS_2 has a wider transparency region compared with GaP and Si and a larger refractive index than TiO_2 (Figure 6). More surprisingly, when we use the refractive index from first-principle calculations (Figure 4a) for monocrystalline SnS_2, it perfectly fits into the correlation line between the refractive indices and optical bandgaps of high refractive index materials (Figure 6c). Therefore, SnS_2 enables the essential spectral range of all-dielectric nanophotonics between GaP and TiO_2.

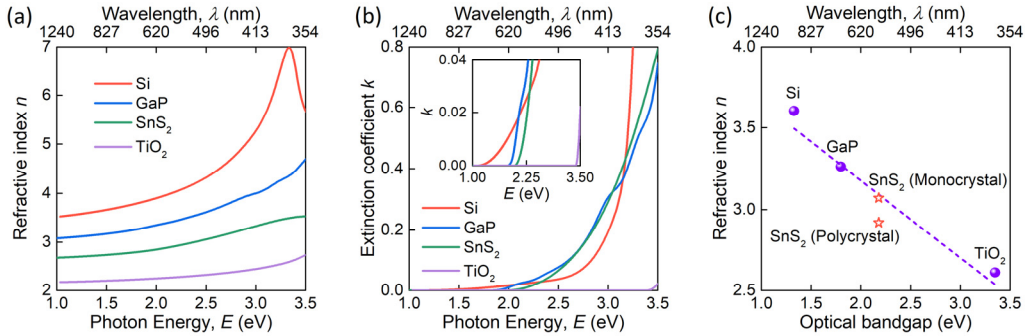

Figure 6. SnS_2 as a high refractive index material. (**a**) Refractive index n and (**b**) extinction coefficient k of SnS_2 compared with other high refractive index materials—Si, GaP, and TiO_2. (**c**) The dependence of refractive index and optical bandgap for high refractive index materials.

3. Materials and Methods

3.1. Materials

CVD-grown full-area coverage SnS_2 and $SnSe_2$ samples of thin films were purchased from 2d Semiconductors Inc. (2d Semiconductors Inc., Scottsdale, AZ, USA). The samples with an area of 1×1 cm^2 were grown by CVD on sapphire substrates and subsequently transferred on quartz substrates.

3.2. Surface Morphology Characterization

The surface morphology of SnS_2 and $SnSe_2$ thin films was analysed by an optical microscope (Nikon LV150, Tokyo, Japan) with a digital camera DS-Fi3, as well as the

scanning electron microscope (SEM) using the acceleration voltage of 30 kV and different magnifications (JEOL JSM-7001F, Tokyo, Japan) to prove films homogeneity. The film surface morphology was studied by atomic force microscopy (AFM, notegra, Nt-MDT Spectrum Instruments, Moscow, Russia) in semi-contact mode using a silicon tip with a radius <10 nm and resonance frequency of ~250 kHz (HA_NC Etalon, Tipsnano, Tallinn, Estonia) to determine surface roughnesses and films thicknesses.

3.3. Crystal Structure Characterization

X-ray diffraction (XRD) characterization was performed by X-ray diffractometer (ARL X'TRA, Thermo Fisher Scientific, Waltham, MA, USA) using Cu $K_{\alpha 1}$ radiation line (λ = 1.54 Å) to analyze the crystal structure of the films using a regime of 2θ-scan with angles range of 5°–75° with a step of 0.05° and accumulation time of 2 s.

3.4. Raman Characterization

The Raman spectra were measured with a confocal scanning Raman microscope Horiba LabRAM HR Evolution (HORIBA Ltd., Kyoto, Japan) with 532 nm linearly polarized excitation laser, 1800 lines/mm diffraction grating, and ×100 objective (N.A. = 0.90) using a spectra range of 100–450 cm^{-1}. The spectra were recorded with 3.5 mW incident laser power, with an integration time of 10 s and 10 spectra accumulation.

3.5. Ellipsometry Analysis

The optical constants n and k of SnS_2 and $SnSe_2$ were measured using a variable-angle spectroscopic ellipsometer (VASE, J.A. Woollam Co., Lincoln, NE, USA), working at room temperature, at variable incidence angles 30°–75° with a step of 5° and wide spectral range from 300 to 3300 nm with a step of 1 nm, having the spotlight of size ~1 mm around the center of the sample, utilizing the high precision optical alignment. To fit the measured ellipsometric parameters Ψ and Δ, we used the Tauc–Lorentz oscillator model was used, defined by the following formula:

$$\varepsilon_2 = \begin{cases} \frac{1}{E} \cdot \frac{AE_0C\left(E-E_g\right)^2}{\left(E^2-E_0^2\right)^2+C^2E^2} & for\ E > E_g \\ 0 & for\ E < E_g \end{cases}, \quad (2)$$

where E is the energy of the photon, A is the oscillator strength, C is the oscillator broadening, E_g is the optical band-gap, E_0 is the oscillator central energy, and the real part of the dielectric function ε_1 was obtained from the imaginary part ε_2 using the Kramers–Kronig integration, plus ε_∞, to account for high energy electronic transitions. For SnS_2, we used one Tauc–Lorentz oscillator with the following parameters: A = 54.613 eV; C = 1.626 eV; E_0 = 3.911 eV; E_g = 1.970 eV and ε_∞ = 5.031. For $SnSe_2$, we used two Tauc–Lorentz oscillators with the following parameters: A_1 = 14.435 eV; C_1 = 1.345 eV; E_{01} = 2.870 eV; A_2 = 20.432 eV; C_2 = 0.875 eV; E_{02} = 3.981 eV; E_g = 0.736 eV and ε_∞ = 4.445.

3.6. Optical Properties Characterization

Optical transmittance spectra of SnS_2 and $SnSe_2$ films on quartz were measured with a spectrophotometer (Cary 5000 UV-Vis-NIR, Agilent Tech., Santa Clara, CA, USA) at a wavelength range of 300–3300 nm.

The nonlinear optical properties of the sample were studied by a home-built multiphoton microscope [69], based on femtosecond Ti:sapphire laser (Coherent Chameleon Ultra 2, Santa Clara city, CA, USA) tunable in the spectral range from 680 to 1080 nm. The laser beam (80 MHz repetition rate, 150 fs pulse duration) was directed through the system, consisting of a half-wave plate on a motorized rotation stage and a Glan–Taylor prism, which provided control of the power and polarization of the incident radiation.

Then, the beam was focused on the sample surface with a 10 cm lens into a 50 μm spot. The sample was mounted on a 3-axis motorized stage (SigmaKoki, Tokyo, Japan) with a

minimum step of 0.1 μm, which made it possible to accurately align the sample relative to the pump spot. The SH radiation generated by the sample was collected by an objective lens (N.A. = 0.95, 100x, Olympus, Tokyo, Japan) and directed to the detection channel consisting of a tube lens, filter (FGB39 Thorlabs, Newton, NJ, USA) to cut off the pump radiation, monochoromator, and a scientific CCD camera (Andor Clara, Belfast, United Kingdom). The SH signal was normalized over spectral functions of all optical elements in the detection channel including objective lens transmittance and detector sensitivity spectra. SHG spectra were measured at the same pump intensity for all wavelengths. The experimental setup was fully automated and situated in a black box.

3.7. First-Principle Calculations

The optical properties of SnS_2 and $SnSe_2$ were calculated using density functional theory (DFT) implemented in the Vienna Ab Initio Simulation Package [70,71]. Core electrons, their interaction with valence electrons, and exchange correlation effects were described within generalized gradient approximation [72] (Perdew–Burke–Ernzerhof functional) and the projector-augmented wave pseudopotentials [73]. The unit cell parameters were $a = b = 3.6486$ Å and $c = 5.8992$ Å for SnS_2 and $a = b = 3.811$ Å and $c = 6.137$ Å for $SnSe_2$. The calculation was performed in two steps: first, the atomic positions of SnS_2 and $SnSe_2$ were relaxed in until the interatomic forces were less than 10^{-3} eV/Å, and a 1-electron basis set was obtained from a standard DFT calculations. Second, the real and imaginary parts of frequency-dependent dielectric function were calculated using the GW approximation [74]. Cutoff energy of the plane waves basis set was set to 600 eV, and the Γ-centered $11 \times 11 \times 7$ k-points mesh was used to sample the first Brillouin zone.

4. Conclusions

In conclusion, we theoretically and experimentally determined the anisotropic optical constants of SnS_2 and $SnSe_2$ in a wide spectral range (300–3300 nm). Our findings reveal a strong dielectric response of SnS_2 and $SnSe_2$ and their broad range with zero absorption. More importantly, for SnS_2, this range includes visible frequencies, which makes SnS_2 a novel high refractive index material, which complements the classical high refractive index materials Si, GaP, and TiO_2. Additionally, we measured the second-order nonlinear susceptibility of SnS_2 and $SnSe_2$. From a broader perspective, our research enables a foundation for advanced optical engineering with SnS_2 and $SnSe_2$.

Author Contributions: V.S.V., A.V.A., A.A.F. and A.A.V. suggested and directed the project; G.A.E., D.I.Y., M.A.E.-S., M.K.T., A.A.P., I.M.A., V.O.B., A.S.S., G.I.T. and S.M.N. performed the measurements and analyzed the data; A.B.M. and I.A.K. provided theoretical support; G.A.E., D.I.Y., M.A.E.-S., M.K.T., A.A.V., A.V.A. and V.S.V. interpreted the experimental results; G.A.E., D.I.Y. and M.A.E.-S. wrote the original draft; G.A.E., D.I.Y., A.A.V., A.V.A. and V.S.V. reviewed and edited the paper; G.A.E., D.I.Y. and M.A.E.-S. contributed equally to this work and should be considered the first co-authors. All authors contributed to the discussions and commented on the paper. All authors have read and agreed to the published version of the manuscript.

Funding: We are gratefully acknowledge the financial support from the Ministry of Science and Higher Education of the Russian Federation (Agreement No. 075-15-2021-987). A.A.P., V.O.B. and A.A.F. acknowledge support by Russian Science Foundation (Grant No. 20-12-00371). G.A.E. acknowledges support by the Fellowship of the President of the Russian Federation to young scientists and postgraduates (SP-2627.2021.5). D.I.Y. acknowledges support by the Fellowship of the President of the Russian Federation to young scientists and postgraduates (SP-1194.2021.5).

Institutional Review Board Statement: Not applicable.

Informed Consent Statement: Not applicable.

Data Availability Statement: The data presented in this study are available upon reasonable request from the corresponding author.

Acknowledgments: The authors thank MIPT's Shared Research Facilities Center for the use of their equipment.

Conflicts of Interest: The authors declare no conflict of interest.

Appendix A

Table A1. Tabulated optical constants for SnS_2 and $SnSe_2$ films from Figure 3a,b.

	SnS_2		$SnSe_2$	
λ (nm)	***n***	***k***	***n***	***K***
300	3.8943	1.0436	2.8895	2.5984
350	3.5319	0.8434	3.8561	1.3915
400	3.3828	0.3664	3.5830	1.1143
450	3.1896	0.1537	3.6856	0.9836
500	3.0450	0.0599	3.7271	0.7105
550	2.9415	0.0180	3.6563	0.4900
600	2.8674	0.0021	3.5609	0.3480
650	2.8171	0.0000	3.4737	0.2566
700	2.7841	0.0000	3.4004	0.1950
750	2.7602	0.0000	3.3399	0.1515
800	2.7420	0.0000	3.2897	0.1195
850	2.7277	0.0000	3.2477	0.0952
900	2.7163	0.0000	3.2122	0.0762
1200	2.6782	0.0000	3.0787	0.0190
1500	2.6621	0.0000	3.0115	0.0021
1800	2.6537	0.0000	2.9751	0.0000
2100	2.6488	0.0000	3.6446	0.0000
2400	2.6456	0.0000	3.6001	0.0000
2700	2.6434	0.0000	3.5663	0.0000
3000	2.6419	0.0000	3.5400	0.0000
3300	2.6408	0.0000	3.5194	0.0000

References

1. Mueller, T.; Xia, F.; Avouris, P. Graphene photodetectors for high-speed optical communications. *Nat. Photonics* **2010**, *4*, 297–301. [CrossRef]
2. Zhang, K.; Feng, Y.; Wang, F.; Yang, Z.; Wang, J. Two dimensional hexagonal boron nitride (2D-hBN): Synthesis, properties and applications. *J. Mater. Chem. C* **2017**, *5*, 11992–12022. [CrossRef]
3. Pi, L.; Li, L.; Liu, K.; Zhang, Q.; Li, H.; Zhai, T. Recent Progress on 2D Noble-Transition-Metal Dichalcogenides. *Adv. Funct. Mater.* **2019**, *29*, 1904932. [CrossRef]
4. Yin, Z.; Li, H.; Li, H.; Jiang, L.; Shi, Y.; Sun, Y.; Lu, G.; Zhang, Q.; Chen, X.; Zhang, H. Single-Layer MoS_2 Phototransistors. *ACS Nano* **2011**, *6*, 74–80. [CrossRef] [PubMed]
5. Mueller, T.; Malic, E. Exciton physics and device application of two-dimensional transition metal dichalcogenide semiconductors. *npj 2D Mater. Appl.* **2018**, *2*, 29. [CrossRef]
6. Thakar, K.; Lodha, S. Optoelectronic and photonic devices based on transition metal dichalcogenides. *Mater. Res. Express* **2020**, *7*, 014002. [CrossRef]
7. Manzeli, S.; Ovchinnikov, D.; Pasquier, D.; Yazyev, O.; Kis, A. 2D transition metal dichalcogenides. *Nat. Rev. Mater.* **2017**, *2*, 17033. [CrossRef]
8. El-Sayed, M.; Ermolaev, G.; Voronin, K.; Romanov, R.; Tselikov, G.; Yakubovsky, D.; Doroshina, N.; Nemtsov, A.; Solovey, V.; Voronov, A.; et al. Optical Constants of Chemical Vapor Deposited Graphene for Photonic Applications. *Nanomaterials* **2021**, *11*, 1230. [CrossRef]
9. Geim, A.K.; Grigorieva, I.V. Van der Waals heterostructures. *Nature* **2013**, *499*, 419–425. [CrossRef] [PubMed]
10. Novoselov, K.S.; Mishchenko, A.; Carvalho, A.; Neto, A.H.C. 2D materials and van der Waals heterostructures. *Science* **2016**, *353*, aac9439. [CrossRef]
11. Verre, R.; Baranov, D.G.; Munkhbat, B.; Cuadra, J.; Käll, M.; Shegai, T. Transition metal dichalcogenide nanodisks as high-index dielectric Mie nanoresonators. *Nat. Nanotechnol.* **2019**, *14*, 679–683. [CrossRef]
12. Munkhbat, B.; Yankovich, A.B.; Baranov, D.G.; Verre, R.; Olsson, E.; Shegai, T.O. Transition metal dichalcogenide metamaterials with atomic precision. *Nat. Commun.* **2020**, *11*, 4604. [CrossRef] [PubMed]

13. Mupparapu, R.; Steinert, M.; George, A.; Tang, Z.; Turchanin, A.; Pertsch, T.; Staude, I. Facile Resist-Free Nanopatterning of Monolayers of MoS_2 by Focused Ion-Beam Milling. *Adv. Mater. Interfaces* **2020**, *7*, 2000858. [CrossRef]
14. Castellanos-Gomez, A.; Barkelid, M.; Goossens, A.M.; Calado, V.E.; van der Zant, H.S.J.; Steele, G.A. Laser-Thinning of MoS_2: On Demand Generation of a Single-Layer Semiconductor. *Nano Lett.* **2012**, *12*, 3187–3192. [CrossRef]
15. Lin, H.; Xu, Z.-Q.; Cao, G.; Zhang, Y.; Zhou, J.; Wang, Z.; Wan, Z.; Liu, Z.; Loh, K.P.; Qiu, C.-W.; et al. Diffraction-limited imaging with monolayer 2D material-based ultrathin flat lenses. *Light. Sci. Appl.* **2020**, *9*, 137. [CrossRef]
16. Mohan, V.B.; Lau, K.-T.; Hui, D.; Bhattacharyya, D. Graphene-based materials and their composites: A review on production, applications and product limitations. *Compos. Part B Eng.* **2018**, *142*, 200–220. [CrossRef]
17. Castellanos-Gomez, A. Why all the fuss about 2D semiconductors? *Nat. Photonics* **2016**, *10*, 202–204. [CrossRef]
18. Caldwell, J.D.; Aharonovich, I.; Cassabois, G.; Edgar, J.H.; Gil, B.; Basov, D.N. Photonics with hexagonal boron nitride. *Nat. Rev. Mater.* **2019**, *4*, 552–567. [CrossRef]
19. Novoselov, K.S.; Geim, A.K.; Morozov, S.V.; Jiang, D.; Zhang, Y.; Dubonos, S.V.; Grigorieva, I.V.; Firsov, A.A. Electric field effect in atomically thin carbon films. *Science* **2004**, *306*, 666–669. [CrossRef] [PubMed]
20. Mak, K.F.; Lee, C.; Hone, J.; Shan, J.; Heinz, T.F. Atomically Thin MoS_2: A New Direct-Gap Semiconductor. *Phys. Rev. Lett.* **2010**, *105*, 136805. [CrossRef]
21. Dean, C.R.; Young, A.; Meric, I.; Lee, C.; Wang, L.; Sorgenfrei, S.; Watanabe, K.; Taniguchi, T.; Kim, P.; Shepard, K.L.; et al. Boron nitride substrates for high-quality graphene electronics. *Nat. Nanotechnol.* **2010**, *5*, 722–726. [CrossRef]
22. Geim, A.K.; Novoselov, K.S. The rise of graphene. *Nat. Mater.* **2007**, *6*, 183–191. [CrossRef]
23. Mounet, N.; Gibertini, M.; Schwaller, P.; Campi, D.; Merkys, A.; Marrazzo, A.; Sohier, T.; Castelli, I.E.; Cepellotti, A.; Pizzi, G.; et al. Two-dimensional materials from high-throughput computational exfoliation of experimentally known compounds. *Nat. Nanotechnol.* **2018**, *13*, 246–252. [CrossRef]
24. Huang, Y.; Xu, K.; Wang, Z.; Shifa, T.A.; Wang, Q.; Wang, F.; Jiang, C.; He, J. Designing the shape evolution of $SnSe_2$ nanosheets and their optoelectronic properties. *Nanoscale* **2015**, *7*, 17375–17380. [CrossRef] [PubMed]
25. Huang, Y.; Sutter, E.; Sadowski, J.; Cotlet, M.; Monti, O.L.; Racke, D.A.; Neupane, M.R.; Wickramaratne, D.; Lake, R.; Parkinson, B.A.; et al. Tin Disulfide—An Emerging Layered Metal Dichalcogenide Semiconductor: Materials Properties and Device Characteristics. *ACS Nano* **2014**, *8*, 10743–10755. [CrossRef] [PubMed]
26. Domingo, G.; Itoga, R.S.; Kannewurf, C.R. Fundamental Optical Absorption in SnS_2 and $SnSe_2$. *Phys. Rev. (Ser. I)* **1966**, *143*, 536–541. [CrossRef]
27. Burton, L.A.; Whittles, T.J.; Hesp, D.; Linhart, W.M.; Skelton, J.M.; Hou, B.; Webster, R.F.; O'Dowd, G.; Reece, C.; Cherns, D.; et al. Electronic and optical properties of single crystal SnS_2: An earth-abundant disulfide photocatalyst. *J. Mater. Chem. A* **2015**, *4*, 1312–1318. [CrossRef]
28. Bertrand, Y.; Leveque, G.; Raisin, C.; Levy, F. Optical properties of $SnSe_2$ and SnS_2. *J. Phys. C Solid State Phys.* **1979**, *12*, 2907–2916. [CrossRef]
29. Bordas, J.; Robertson, J.; Jakobsson, A. Ultraviolet properties and band structure of SnS_2, $SnSe_2$, CdI_2, PbI_2, BiI_3 and BiOI crystals. *J. Phys. C Solid State Phys.* **1978**, *11*, 2607–2621. [CrossRef]
30. Mandalidis, S.; Kalomiros, J.; Kambas, K.; Anagnostopoulos, A.N. Optical investigation of SnS_2 single crystals. *J. Mater. Sci.* **1996**, *31*, 5975–5978. [CrossRef]
31. Song, H.S.; Li, S.L.; Gao, L.; Xu, Y.; Ueno, K.; Tang, J.; Cheng, Y.B.; Tsukagoshi, K. High-performance top-gated monolayer SnS_2 field-effect transistors and their integrated logic circuits. *Nanoscale* **2013**, *5*, 9666–9670. [CrossRef] [PubMed]
32. Su, G.; Hadjiev, V.; Loya, P.E.; Zhang, J.; Lei, S.; Maharjan, S.; Dong, P.; Ajayan, P.M.; Lou, J.; Peng, H. Chemical Vapor Deposition of Thin Crystals of Layered Semiconductor SnS_2 for Fast Photodetection Application. *Nano Lett.* **2014**, *15*, 506–513. [CrossRef] [PubMed]
33. Su, Y.; Ebrish, M.A.; Olson, E.J.; Koester, S.J. $SnSe_2$ field-effect transistors with high drive current. *Appl. Phys. Lett.* **2013**, *103*, 263104. [CrossRef]
34. Tan, F.; Qu, S.; Wu, J.; Liu, K.; Zhou, S.; Wang, Z. Preparation of SnS_2 colloidal quantum dots and their application in organic/inorganic hybrid solar cells. *Nanoscale Res. Lett.* **2011**, *6*, 298. [CrossRef] [PubMed]
35. Bai, Y.; Zong, X.; Yu, H.; Chen, Z.-G.; Wang, L. Scalable Low-Cost SnS_2 Nanosheets as Counter Electrode Building Blocks for Dye-Sensitized Solar Cells. *Chem. Eur. J.* **2014**, *20*, 8670–8676. [CrossRef]
36. Biswas, R.; Dandu, M.; Prosad, A.; Das, S.; Menon, S.; Deka, J.; Majumdar, K.; Raghunathan, V. Strong near band-edge excited second-harmonic generation from multilayer 2H Tin diselenide. *Sci. Rep.* **2021**, *11*, 15017. [CrossRef]
37. Yang, H.R.; Liu, X.M. Nonlinear optical response and applications of tin disulfide in the near- and mid-infrared. *Appl. Phys. Lett.* **2017**, *110*, 171106. [CrossRef]
38. Lu, H.; Wang, Z.; Huang, Z.; Tao, J.; Xiong, H.; Qiu, W.; Guan, H.; Dong, H.; Dong, J.; Zhu, W.; et al. Resonance-assisted light–control–light characteristics of SnS_2 on a microfiber knot resonator with fast response. *Photonics Res.* **2018**, *6*, 1137–1143. [CrossRef]
39. Müller, M.; Zentel, R.; Maka, T.; Romanov, S.G.; Sotomayor Torres, C.M. Photonic Crystal Films with High Refractive Index Contrast. *Adv. Mater.* **2000**, *12*, 1499–1503. [CrossRef]
40. Jin, Y.; Zhu, Y.; Yang, X.; Jiang, H.; Li, C. In situ synthesis of sulfide-coated polystyrene composites for the fabrication of photonic crystals. *J. Colloid Interface Sci.* **2006**, *301*, 130–136. [CrossRef] [PubMed]

41. Gao, W.; Zheng, Z.; Li, Y.; Zhao, Y.; Xu, L.; Deng, H.; Li, J. High performance tin diselenide photodetectors dependent on thickness: A vertical graphene sandwiched device and interfacial mechanism. *Nanoscale* **2019**, *11*, 13309–13317. [CrossRef]
42. Fan, C.; Liu, Z.; Yuan, S.; Meng, X.; An, X.; Jing, Y.; Sun, C.; Zhang, Y.; Zhang, Z.; Wang, M.; et al. Enhanced Photodetection Performance of Photodetectors Based on Indium-Doped Tin Disulfide Few Layers. *ACS Appl. Mater. Interfaces* **2021**, *13*, 35889–35896. [CrossRef]
43. Joseph, A.; Anjitha, C.; Aravind, A.; Aneesh, P. Structural, optical and magnetic properties of SnS_2 nanoparticles and photo response characteristics of p-Si/n-SnS_2 heterojunction diode. *Appl. Surf. Sci.* **2020**, *528*, 146977. [CrossRef]
44. Smith, A.J.; Meek, P.E.; Liang, W.Y. Raman scattering studies of SnS_2 and $SnSe_2$. *J. Phys. C Solid State Phys.* **1977**, *10*, 1321–1323. [CrossRef]
45. Mitchell, R.S.; Fujiki, Y.; Ishizawa, Y. Structural polytypism of SnS_2. *Nature* **1974**, *247*, 537–538. [CrossRef]
46. Gonzalez, J.M.; Oleynik, I.I. Layer-dependent properties of SnS_2 and $SnSe_2$ two-dimensional materials. *Phys. Rev. B* **2016**, *94*, 125443. [CrossRef]
47. Lin, D.-Y.; Hsu, H.-P.; Tsai, C.-F.; Wang, C.-W.; Shih, Y.-T. Temperature Dependent Excitonic Transition Energy and Enhanced Electron-Phonon Coupling in Layered Ternary $SnS_{2-x}Se_x$ Semiconductors with Fully Tunable Stoichiometry. *Molecules* **2021**, *26*, 2184. [CrossRef] [PubMed]
48. Lin, G.; Zheng, T.; Zhan, L.; Lu, J.; Huang, J.; Wang, H.; Zhou, Y.; Zhang, X.; Cai, W. Tunable structure and optical properties of single crystal SnS_2 flakes. *Appl. Phys. Express* **2020**, *13*, 035504. [CrossRef]
49. Shown, I.; Samireddi, S.; Chang, Y.-C.; Putikam, R.; Chang, P.-H.; Sabbah, A.; Fu, F.-Y.; Chen, W.-F.; Wu, C.-I.; Yu, T.-Y.; et al. Carbon-doped SnS_2 nanostructure as a high-efficiency solar fuel catalyst under visible light. *Nat. Commun.* **2018**, *9*, 169. [CrossRef]
50. Lee, N.; Lee, G.; Choi, H.; Park, H.; Choi, Y.; Seo, H.; Ju, H.; Kim, S.; Sul, O.; Lee, J.; et al. Layered deposition of SnS_2 grown by atomic layer deposition and its transport properties. *Nanotechnology* **2019**, *30*, 405707. [CrossRef]
51. Zhang, Y.; Shi, Y.; Wu, M.; Zhang, K.; Man, B.; Liu, M. Synthesis and Surface-Enhanced Raman Scattering of Ultrathin $SnSe_2$ Nanoflakes by Chemical Vapor Deposition. *Nanomaterials* **2018**, *8*, 515. [CrossRef]
52. Ermolaev, G.A.; Yakubovsky, D.I.; Stebunov, Y.V.; Arsenin, A.V.; Volkov, V.S. Spectral ellipsometry of monolayer transition metal dichalcogenides: Analysis of excitonic peaks in dispersion. *J. Vac. Sci. Technol. B* **2020**, *38*, 014002. [CrossRef]
53. Ermolaev, G.; El-Sayed, M.; Yakubovsky, D.; Voronin, K.; Romanov, R.; Tatmyshevskiy, M.; Doroshina, N.; Nemtsov, A.; Voronov, A.; Novikov, S.; et al. Optical Constants and Structural Properties of Epitaxial MoS_2 Monolayers. *Nanomaterials* **2021**, *11*, 1411. [CrossRef]
54. Ermolaev, G.A.; Voronin, K.V.; Tatmyshevskiy, M.K.; Mazitov, A.B.; Slavich, A.S.; Yakubovsky, D.I.; Tselin, A.P.; Mironov, M.S.; Romanov, R.I.; Markeev, A.M.; et al. Broadband Optical Properties of Atomically Thin PtS_2 and $PtSe_2$. *Nanomaterials* **2021**, *11*, 3269. [CrossRef]
55. Jellison, G.E.; Modine, F.A. Parameterization of the optical functions of amorphous materials in the interband region. *Appl. Phys. Lett.* **1996**, *69*, 371–373. [CrossRef]
56. Ermolaev, G.A.; Stebunov, Y.V.; Vyshnevyy, A.A.; Tatarkin, D.E.; Yakubovsky, D.I.; Novikov, S.M.; Baranov, D.G.; Shegai, T.; Nikitin, A.Y.; Arsenin, A.V.; et al. Broadband optical properties of monolayer and bulk MoS2. *npj 2D Mater. Appl.* **2020**, *4*, 21. [CrossRef]
57. Niu, Y.; Gonzalez-Abad, S.; Frisenda, R.; Marauhn, P.; Drüppel, M.; Gant, P.; Schmidt, R.; Taghavi, N.S.; Barcons, D.; Molina-Mendoza, A.J.; et al. Thickness-Dependent Differential Reflectance Spectra of Monolayer and Few-Layer MoS_2, $MoSe_2$, WS_2 and WSe_2. *Nanomaterials* **2018**, *8*, 725. [CrossRef] [PubMed]
58. Passler, N.C.; Paarmann, A. Generalized 4 × 4 matrix formalism for light propagation in anisotropic stratified media: Study of surface phonon polaritons in polar dielectric heterostructures. *J. Opt. Soc. Am. B* **2017**, *34*, 2128–2139. [CrossRef]
59. Ermolaev, G.A.; Tsapenko, A.P.; Volkov, V.S.; Anisimov, A.S.; Gladush, Y.G.; Nasibulin, A.G. Express determination of thickness and dielectric function of single-walled carbon nanotube films. *Appl. Phys. Lett.* **2020**, *116*, 231103. [CrossRef]
60. Ermolaev, G.A.; Grudinin, D.V.; Stebunov, Y.V.; Voronin, K.V.; Kravets, V.G.; Duan, J.; Mazitov, A.B.; Tselikov, G.I.; Bylinkin, A.; Yakubovsky, D.I.; et al. Giant optical anisotropy in transition metal dichalcogenides for next-generation photonics. *Nat. Commun.* **2021**, *12*, 854. [CrossRef]
61. Niu, K.; Chen, Q.; Sun, R.; Man, B.; Zhang, H. Passively Q-switched erbium-doped fiber laser based on SnS_2 saturable absorber. *Opt. Mater. Express* **2017**, *7*, 3934–3943. [CrossRef]
62. Boyd, R.W. *Nonlinear Optics*; Elsevier: Amsterdam, The Netherlands, 2003; ISBN 9780121216825.
63. Evlyukhin, A.B.; Novikov, S.M.; Zywietz, U.; Eriksen, R.L.; Reinhardt, C.; Bozhevolnyi, S.I.; Chichkov, B.N. Demonstration of Magnetic Dipole Resonances of Dielectric Nanospheres in the Visible Region. *Nano Lett.* **2012**, *12*, 3749–3755. [CrossRef]
64. Baranov, D.G.; Zuev, D.A.; Lepeshov, S.I.; Kotov, O.V.; Krasnok, A.E.; Evlyukhin, A.B.; Chichkov, B.N. All-dielectric nanophotonics: The quest for better materials and fabrication techniques. *Optica* **2017**, *4*, 814–825. [CrossRef]
65. Khmelevskaia, D.; Markina, D.I.; Fedorov, V.V.; Ermolaev, G.A.; Arsenin, A.V.; Volkov, V.S.; Goltaev, A.S.; Zadiranov, Y.M.; Tzibizov, I.A.; Pushkarev, A.P.; et al. Directly grown crystalline gallium phosphide on sapphire for nonlinear all-dielectric nanophotonics. *Appl. Phys. Lett.* **2021**, *118*, 201101. [CrossRef]
66. Herzinger, C.M.; Johs, B.D.; McGahan, W.A.; Woollam, J.A.; Paulson, W.M. Ellipsometric determination of optical constants for silicon and thermally grown silicon dioxide via a multi-sample, multi-wavelength, multi-angle investigation. *J. Appl. Phys.* **1998**, *83*, 3323–3336. [CrossRef]

67. Tiwald, T.E.; Schubert, M. Measurement of rutile TiO_2 dielectric tensor from 0.148 to 33 μm using generalized ellipsometry. *Opt. Diagn. Methods Inorg. Mater. II* **2000**, *4103*, 19–29.
68. Ermolaev, G.; Kushnir, S.E.; Sapoletova, N.A.; Napolskii, K.S. Titania Photonic Crystals with Precise Photonic Band Gap Position via Anodizing with Voltage versus Optical Path Length Modulation. *Nanomaterials* **2019**, *9*, 651. [CrossRef] [PubMed]
69. Popkova, A.A.; Antropov, I.M.; Fröch, J.E.; Kim, S.; Aharonovich, I.; Bessonov, V.O.; Solntsev, A.S.; Fedyanin, A.A. Optical Third-Harmonic Generation in Hexagonal Boron Nitride Thin Films. *ACS Photon* **2021**, *8*, 824–831. [CrossRef]
70. Kresse, G.; Furthmüller, J. Efficient iterative schemes forab initiototal-energy calculations using a plane-wave basis set. *Phys. Rev. B* **1996**, *54*, 11169–11186. [CrossRef]
71. Kresse, G.; Furthmüller, J. Efficiency of ab-initio total energy calculations for metals and semiconductors using a plane-wave basis set. *Comput. Mater. Sci.* **1996**, *6*, 15–50. [CrossRef]
72. Perdew, J.P.; Burke, K.; Ernzerhof, M. Generalized gradient approximation made simple. *Phys. Rev. Lett.* **1996**, *77*, 3865–3868. [CrossRef] [PubMed]
73. Kresse, G.; Joubert, D. From ultrasoft pseudopotentials to the projector augmented-wave method. *Phys. Rev. B* **1999**, *59*, 1758. [CrossRef]
74. Shishkin, M.; Kresse, G. Implementation and performance of the frequency-dependentGWmethod within the PAW framework. *Phys. Rev. B* **2006**, *74*, 035101. [CrossRef]